# High-resolution measurements of the *K-MM* radiative Auger effect in medium-mass atoms

Ch. Herren and J.-Cl. Dousse
*Physics Department, University of Fribourg, CH-1700 Fribourg, Switzerland*
(Received 12 September 1995)

High-resolution measurements of the $K\beta_{1,3}$ low-energy satellites of $_{42}$Mo, $_{44}$Ru, $_{46}$Pd, $_{48}$Cd, and $_{50}$Sn were performed. The photoinduced x-ray spectra were measured with a transmission-type bent-crystal spectrometer. Particular groups of *K-MM* radiative Auger effect (RAE) transitions could be identified. The intensity ratios $I(K\text{-}MM$ RAE$)$ / $I(K\beta_{13})$ were extracted. They are compared to relativistic Hartree-Fock theoretical predictions of Scofield. The experimental energies of the RAE edges are compared to calculated Auger transition energies. The present experiment provides experimental RAE results for solid elements with $Z \geqslant 42$.

PACS number(s): 32.30.Rj, 32.70.Fw, 32.80.Hd, 32.80.Dz

## I. INTRODUCTION

The study of multielectron phenomena in which the interaction between the particles cannot be completely described by an average potential is a field of major interest in inner-shell atomic physics. In particular, the effect of the multielectron interaction on the core-level transitions is not yet fully understood and needs further experimental and theoretical investigations. In this respect the radiative Auger effect (RAE) can provide valuable and rich information. It has to be noted, however, that a better understanding of the radiative Auger mechanisms is not only required for the study of the above mentioned fundamental processes but is also highly desirable in various applications. For instance, regarding the $I(K\beta)$ / $I(K\alpha)$ x-ray yield ratios, which are important in trace element analysis and in methods like proton-induced x-ray emission (PIXE) and x-ray fluorescence (XRF), there are still discrepancies between the experimental values and the theoretical predictions. The differences could be explained, at least partly, by a better knowledge of the RAE intensities [1]. A similar statement can be made for x-ray photoelectron spectroscopy (XPS) in which a more precise knowledge of the RAE line shapes would be also very helpful [2–4].

When an electron is knocked out of the *K* shell–for instance by x-ray bombardment–the reorganization of the atom can take place by different processes. If the *K* hole is filled by an outer electron, let us say an *L* electron, this gives rise to the emission of a fluorescence x ray, a so-called $K\alpha$-diagram line [see Fig. 1(a)]. The reorganization of the atom can also take place without emission of an x ray. In this case the *K* vacancy is filled by an outer electron and the energy is transferred to another bound electron, which is ejected. This process is called an Auger transition [Fig. 1(b)].

Besides these purely radiative and nonradiative deexcitation processes, Bloch [5,6] proposed that there may be an alternative deexcitation mode for a vacancy, in which the excited atom decays by emitting simultaneously an x-ray photon and a valence shell electron instead of undergoing a forbidden quadrupole transition. In this case, the transition energy is shared between the electron and the photon. This process, named radiative Auger effect or the ''inner-shell Compton effect,'' was first observed by Åberg and Utriainen [7], who found that RAE is also possible in the case of an allowed dipole transition.

It was further shown by Åberg [8] that an RAE transition may even occur, in which an inner-shell electron instead of a valence electron is ejected, as depicted in Fig. 1(c). This takes place as a consequence of the sudden change in the average potential acting on the electrons when the inner-shell vacancy moves to an outer shell. If the *K* vacancy is filled by an $M_i$ electron and an $M_j$ electron plus an x ray are simultaneously emitted, the transition is called $K\text{-}M_iM_j$ RAE. As the energy is shared between the electron and the photon, the *K-MM* RAE results in a satellite structure on the low energy side of the diagram line $K\beta$ and the x-ray energy is given by

$$h\nu = E(K - M_iM_j) - E_{kin}(M_j), \tag{1}$$

where the first term represents the energy of the Auger electron and the second the kinetic energy of the $M_j$ electron. The kinetic energy of the electron can take values from zero to $E(K\text{-}M_iM_j)$. Consequently, the energy of the emitted photons corresponds to a continuous distribution, with a maximum value of $E(K\text{-}M_iM_j)$ when the kinetic energy of the electron is zero; this maximum energy appears in the spectrum as a sharp edge smeared out by the instrumental resolution. Since the highest intensity of an RAE transition is observed at the edge energy, one can conclude that most of the ejected electrons have very small kinetic energies [9]. For a solid this means that the electron excited into the continuum by an RAE transition lies just above the Fermi sur-

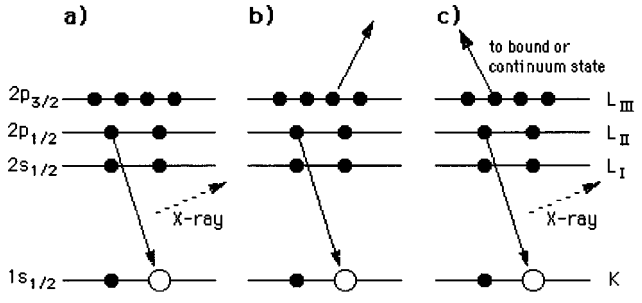


FIG. 1. Schematic representation of possible deexcitation processes of a *K*-shell vacancy: (a) fluorescence; (b) Auger; (c) radiative Auger.

 

face. It is also possible that the electron is promoted to a higher unfilled subshell (shakeup) instead of the continuum (shakeoff). For inner-shell electrons the shakeoff process is dominant, while the shakeup process becomes important for outer-shell electrons.

Furthermore, Åberg [8,10] showed that the radiative Auger transition strength vanishes if one assumes the electrons to be in frozen orbitals; hence, the existence of low-energy satellites clearly indicates that the relaxation of orbitals between the initial and final states should be included in theory. This was done by Scofield in his RHF work, which took proper account of overlap and exchange effects [11].

The principal aim of the present work is to extend the available data set of *K-MM* RAE intensities to the region $42 \leqslant Z \leqslant 50$. To our knowledge, the *K-MM* RAE intensities of solid elements with $Z$ above 35 were measured for the first time. This is probably due to the weak intensities of the RAE transitions and to the fact that these satellites lie in the low energy tails of the strong $K\beta_{1,3}$ diagram lines and are thus difficult to extract. In addition, high resolution measurements of RAE spectra are scarce, because very long aquisition times are needed for measurements with high resolving instruments. Further, the second objective of the present study is to compare the observed RAE edge energies to calculated Auger transition energies [12].

## II. EXPERIMENTAL SETUP

The measurements of the RAE x-ray spectra were performed at the University of Fribourg with a transmission-type bent crystal spectrometer. A detailed description of a similar spectrometer–installed at the Paul Scherrer Institute (PSI) in Villigen, Switzerland–can be found in [13]. The instrument was operated in the modified DuMond-slit geometry [13], which is represented schematically in Fig. 2. This geometry has the advantage that thermal deformations of the target do not influence the line shapes in the measured spectra. In the present experiment the slit was 20 mm high and 0.15 mm wide and placed in front of the targets at a distance of 1.75 cm.

The x-ray emission was induced by means of a commercial 3 kW x-ray tube with an Au anode and a window sheet of nonporous beryllium. The water-cooled tube was operated at 80 kV and 30 mA. It was oriented so that the ionizing radiation was perpendicular to the target-crystal direction. The distance between the tube and the target was 45 mm.

The ruthenium target was made by gluing the Ru powder ($45\mu \leqslant$ particle size $\leqslant 400\mu$) on an aluminum backing as depicted in Fig. 3(a). The other targets were self-supported metallic foils–25 mm high and 4 mm wide–which were mounted on a special holder [Fig. 3(b)]. The thicknesses of the metallic targets were 54.0 mg/cm$^2$ (Mo), 56.5 mg/cm$^2$ (Pd), 45.4 mg/cm$^2$ (Cd), and 40.2 mg/cm$^2$ (Sn). All targets were tilted at about 10° with regard to the target-crystal direction.

A $10 \times 10$ cm$^2$ $SiO_2$ analyzing crystal plate ($d = 2.4567$ Å) of 1 mm thickness was used. The crystal plate was bent cylindrically to a radius of curvature of 3.15 m by means of a method similar to the one described in [14]. The reflecting area was about $5 \times 5$ cm$^2$ and the (110) reflecting planes were used. In order to obtain a good resolution the slit-to-crystal distance should be adjusted for each x-ray line. However, if one wants to measure weak lines over a large angular range, it is more convenient to perform the measurements with an average value of the focusing distance. For this reason, for each target a single focusing distance corresponding to the center of the RAE region was chosen.

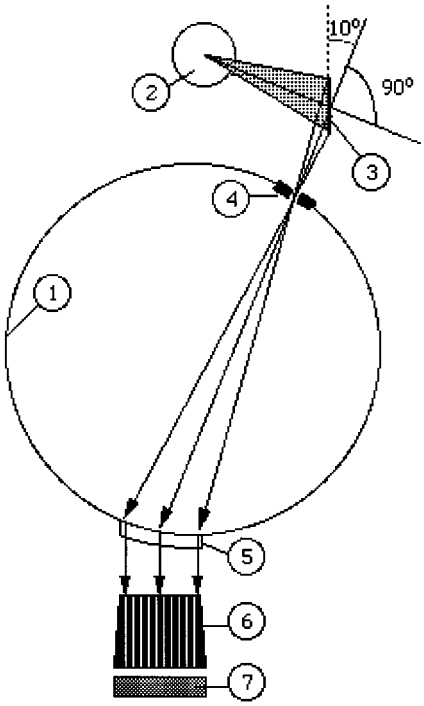


FIG. 2. Schematic representation of the setup of the transmission type bent crystal spectrometer (not to scale). 1, Rowland or focal circle; 2, x-ray tube; 3, target; 4, slit; 5, bent crystal; 6, Soller slit collimator; 7, Phoswich detector.

The x-ray detector was a 5-in.-diam. two-component Phoswich-scintillation counter, consisting of a thin (0.25 in.) NaI(Tl) crystal followed by an optically coupled thick (2 in.) CsI(Tl) crystal. Both crystals were mounted on the same photomultiplier tube. As the rising time of the signal is different for the two crystals, the events corresponding to each scintillation can be identified by pulse shape analysis [15]. In

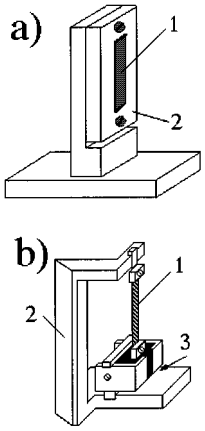


FIG. 3. Geometry of target holders: (a) ruthenium and $MoO_3$ targets, (b) other targets. 1, target; 2, target holder; 3, spring (not visible, between bottom and target).

fact, the signals of the rear CsI crystal were used as anticoincident gate pulses for the analog-to-digital converter (ADC) performing the pulse height analysis of the NaI signals. As photons suffering a Compton scattering in the front detector also produce a signal in the rear detector, they can thus be eliminated. With the x-ray tube switched off, the background measured by the Phoswich detector was found to be almost constant above 20 keV and equal to 0.0015 counts $\mathrm{keV}^{-1}$ $\mathrm{sec}^{-1}$. With a standard 5-in.-in-diameter $\times$ 0.5-in.-thick NaI(Tl) scintillation detector, the average background was approximately four times greater, proving thus the quality of the Compton suppression of the Phoswich detector. The pulse corresponding to the front NaI crystal was further sorted by setting an appropriate energy window in the ADC spectrum, which resulted in an additional reduction of the background events. Since for all the elements investigated in the present experiment the energy differences between the lower limits of the scanned RAE regions and the corresponding $K\beta_{1,3}$ transitions do not exceed 1.5 keV, the detector efficiency was assumed to be constant within these narrow energy intervals. Escape peaks that could affect significantly the detector efficiency did not have to be considered in our study because they are only observed above 33.170 keV ($K$ edge of I), i.e. at higher energies than the ones of our RAE spectra.

Except for Sn, all targets were measured in first order of reflection. As an absorption edge of instrumental origin was observed in the first order spectrum of Sn, this element was measured in second order. The time needed for the measurement of the RAE spectrum was approximately one week for each target. Since intensity fluctuations of the x-ray tube cannot be excluded *a priori* for such long measuring periods, all measurements were performed in several (9–14) successive step-by-step scans. The scans consisted of 120 points with an acquisition time of 400 sec per point. Between each scan, a control measurement of the $K\beta_{1,3}$ diagram line was performed. The aim of these $K\beta_{1,3}$ measurements was to normalize *a posteriori* the intensity of the preceding RAE scan and to adjust, if necessary, the energy scale with respect to the first scan. However, the analysis showed that the fluctuations of the $K\beta_1$ line intensity were smaller than 1%. Similarly, the standard deviation of the average energy of the $K\beta_1$ centroids was found to be less than 0.5 eV. No correction was therefore performed and for each target the total RAE spectrum was built up by summing off-line all scans.

The reflection angles were measured by means of a Doppler shift laser interferometer [13]. The energy calibration of the RAE spectra was achieved by measuring the $K\beta_{1,3}$ lines on both sides of reflection and using the energy of the $K\beta_1$ transitions quoted by Bearden [16].

## III. DATA ANALYSIS

All spectra were analyzed by means of a least-squares-fitting computer program (package MINUIT [17], CERN Library PACKLIB) using Voigt profiles for the transition lines. The Voigt profiles $V(E)$ were constructed by convoluting the natural line shape, which is given according to Weisskopf-Wigner's theory by a Lorentzian function $L(E)$, with the Gaussian instrumental response $G(E)$ of the spectrometer:

TABLE I. Comparison of our experimental $I(K\beta_3)/I(K\beta_1)$ intensity ratios with theoretical predictions from Scofield [31].

| Element | Ratio $\frac{I(K\beta_3)}{I(K\beta_1)}$ Experimental | Theoretical |
|---|---|---|
| $_{42}$Mo | 0.518 ± 0.005 | 0.514 |
| $_{44}$Ru | 0.517 ± 0.003 | 0.514 |
| $_{46}$Pd | 0.514 ± 0.005 | 0.514 |
| $_{48}$Cd | 0.516 ± 0.002 | 0.515 |
| $_{50}$Sn | 0.513 ± 0.004 | 0.515 |

$$V(E)=\lim_{n\to\infty}\int_{-n}^{+n}L(E-E')G(E')dE'$$
$$=\lim_{n\to\infty}\int_{-n}^{+n}\frac{A}{\left(\frac{1}{2}\Gamma\right)^2+(E-E'-E_o)^2}\times\exp(-(E')^2/2\sigma^2)dE', \quad (2)$$

where $A$ gives the peak amplitude, $E_0$ the energy of its centroid, $\Gamma$ the Lorentzian full width at half maximum (FWHM), and $\sigma$ the standard deviation of the Gaussian distribution, related to its FWHM by $\mathrm{FWHM}=2\sqrt{2\ \ln(2)}\sigma$. The function $V(E)$ was evaluated numerically by means of the complex error function method [18,19].

The Gaussian instrumental response depends mainly on the slit width, the crystal mosaicity, and the precision of the crystal curvature. It was determined by measuring the 63.12081 keV [20] $\gamma$-ray of a $^{169}$Yb radioactive source. The $^{169}$Yb measurements were performed in second and third orders of reflection, i.e., at similar Bragg angles as the RAE ones. For both orders a FWHM of about 11.5 arcsec was found for the angular resolution $\Gamma_\theta$. The FWHM energy resolution $\Gamma_E$ is related to $\Gamma_\theta$ by the following equation:

$$\Gamma_E=E\ \cot(\theta)\Gamma_\theta, \quad (3)$$

where $E$ represents the energy of the $\gamma$ or x ray and $\theta$ the corresponding Bragg angle. From (3) one finds that the instrumental energy resolution for the measured RAE regions varied from about 8.5 eV for Mo to about 18 eV for Sn. However, since our measurements were performed with an average focusing distance corresponding to the center of the RAE spectrum, a slightly worse resolution resulted.

The analysis of each spectrum was carried out in three steps.

(i) We analyzed first the $K\beta_{1,3}$ diagram spectrum, using one Voigt function for each transition. The instrumental resolution was taken from (3) with $\Gamma_\theta$=11.5 arcsec, whereas the energies, natural linewidths, and intensities of the $K\beta_1$ and $K\beta_3$ transitions were free fitting parameters. A constant background which was measured outside the energy region of interest was also taken into account in the fitting procedure. The obtained $I(K\beta_3)$ / $I(K\beta_1)$ intensity ratios are listed in Table I, where they are compared to theoretical predictions of Scofield [31]. As can be seen, very good agreement was found for all targets.

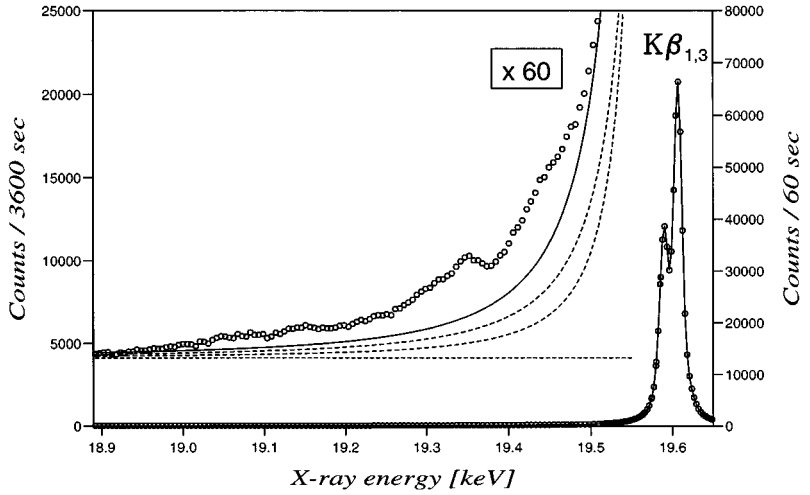


FIG. 4. $K\beta_{1,3}$ spectrum and enlarged tail of $_{42}$Mo. The scale on the right-hand side corresponds to the diagram lines, the one on the left to the tail measurement. The dotted lines show the constant background and the tails of the diagram lines $K\beta_{1,3}$, and the solid line shows the sum of those.

(ii) From the measured total RAE spectrum we then subtracted then the low energy tails of the $K\beta_1$ and $K\beta_3$ lines and the constant background, using the values obtained in the first step of the analysis. The intensities of the $K\beta_1$ and $K\beta_3$ transitions and the background value were of course corrected before the subtraction, to account for the different acquisition times used in the measurements of the $K\beta_{1,3}$ and RAE spectra. The contribution of the $K\beta_{1,3}$ tails and background to the yields observed in the $K$-$MM$ RAE region of Mo is shown for illustration in Fig. 4.

(iii) Finally, the residual spectrum was analyzed. Because theoretical profiles of RAE transitions are difficult to determine, the same fitting method as the one used for the $K\beta_{1,3}$ spectrum was chosen. However, in order to reproduce the asymmetric shape of the RAE transitions, each RAE component was fitted with several Voigt functions. The number of Voigt profiles used to analyze the RAE structures varied from 1 (for weak transitions) to 4 (for the strongest ones) per transition group. However, for all targets, the number of profiles employed to fit a whole RAE spectrum did not exceed 11. The fitted RAE spectra are shown in Figs. 5(a)–5(e). To illustrate the goodness of the fits, the residuals between the observed and fitted spectrum of Ru are represented in Fig. 6.

## IV. RESULTS AND DISCUSSION

### A. Processes competitive with RAE

In the region lying on the low energy side of the $K\beta_{1,3}$ transitions, processes other than RAE can contribute to the observed intensity. Whether such additional effects are important or not is strongly dependent on the atomic number of the observed element. Below, we give a short discussion about possible contributing effects.

#### *1. Radiative electron rearrangement*

A first process which could contribute to the intensity of the $K\beta_{1,3}$ low-energy tail is the radiative electron rearrangement (RER). In the RER process a two-hole initial state decays through a rearrangement of electrons, accompanied by the emission of a photon. Thus, the RER process requires an additional hole in an upper shell. It was shown that RER is negligibly small compared to RAE for elements with $Z \leqslant 30$ [21,22]. In our case, an additional vacancy following a $K$-shell photoionization can only be produced via a shake process. Since the shake probability decreases with growing $Z$ the RER process can be thus certainly neglected for the elements ($42 \leqslant Z \leqslant 50$) investigated in the present study. In addition, the RER intensity would be concentrated in sharp lines instead of an extended structure and could thus be identified by the line profile.

#### *2. Raman scattering*

Another possible process which could affect our spectra is the x-ray Raman scattering which resembles the RAE [23,24]. In this process the x ray emitted as a result of a $K$-shell photoionization scatters inelastically on a neighboring atom. The energy of the scattered photon is equal to its energy before the collision minus the binding energy of the ionized outer-shell electron. It was shown, however, by Keski and Servomaa [25,26] and more recently by Kawai [27], that Raman scattering is also negligibly small compared to RAE. Furthermore Raman lines have symmetric line shapes and could thus also be identified by their profiles.

#### *3. Other processes*

The RAE region might also be affected by $K\alpha$ hypersatellites. The probability for a $K$-shell shakeoff process following a $K$-shell photoionization is, however, extremely small for medium-mass atoms. Calculations based on the sudden approximation and using nonrelativistic Hartree-Fock-Slater (HFS) wave functions were performed for the elements from $Z=2$ to $Z=36$ by Mukoyama and Taniguchi giving for the heaviest element a probability of only $2 \times 10^{-5}$ [28]. In addition, since for our targets the $K\alpha$ hypersatellites lie below the observed RAE energy region [29,30], only the high-energy tails of the very weak hypersatellites could affect the $K$-$MM$ RAE spectra, which is obviously highly improbable.

For Mo, Ru, and Pd the forbidden $K$-$M1$ transitions lie in the region of the $K$-$M_{4,5}M_{4,5}$ RAE. However, one cannot expect a significant contribution from these transitions because they are much weaker than the RAE ones (for instance, less than 0.2% of the whole $K$-$MM$ intensity for Pd) [31].

As the recorded RAE spectra cover a wide domain in energy, they may be contaminated by the x-ray emission

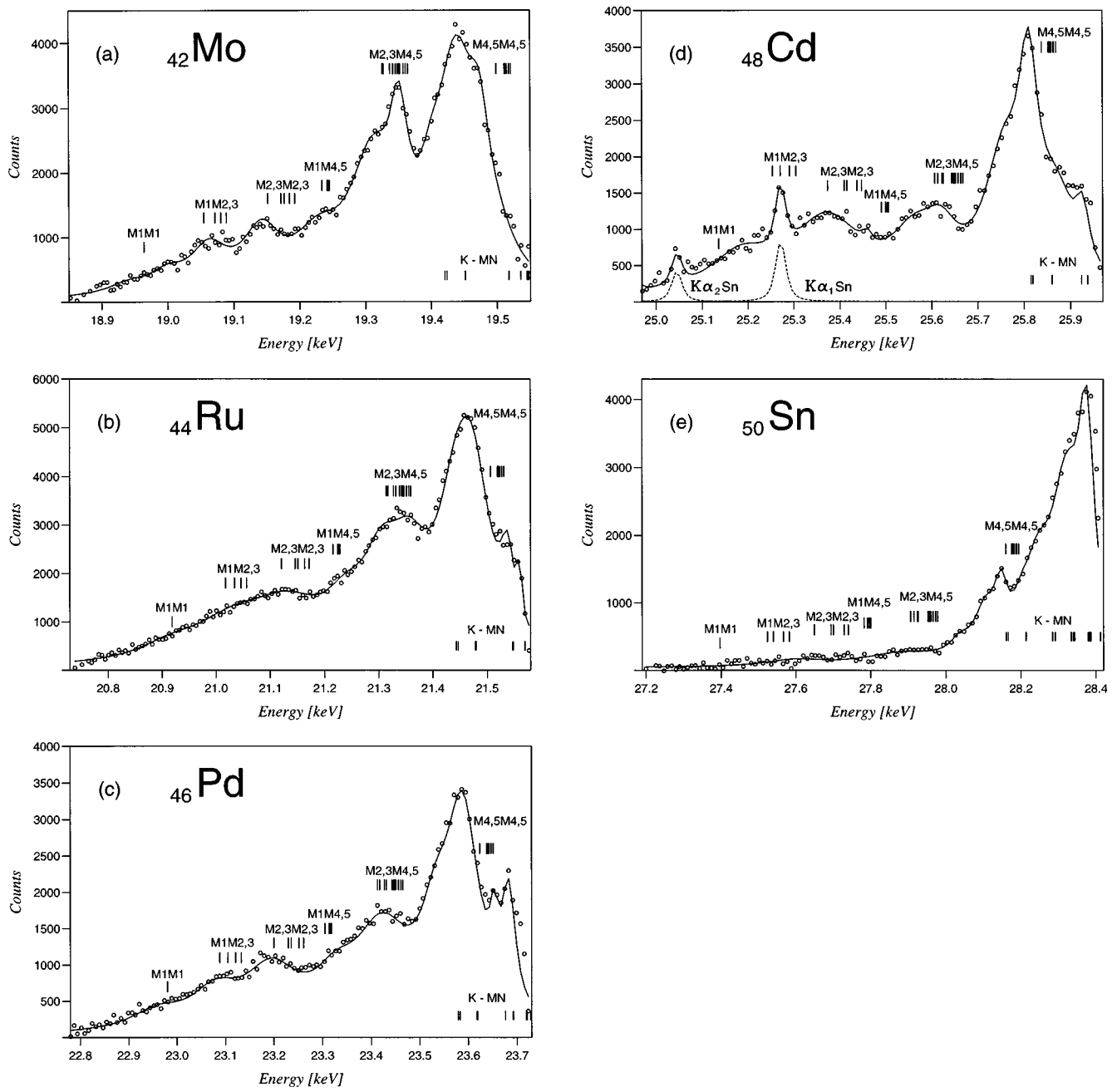


FIG. 5. *K-MM* RAE spectra of the measured targets. Each spectrum was normalized to an acquisition time of 3000 sec per point. The small bars represent theoretical Auger energies from Ref. [12]. Note that these spectra are the subtracted spectra obtained by the procedure described in Sec. III.

from trace elements present in the target material. Such contamination peaks may also be due to a coherent scattering by the target of characteristic x-ray lines from the impurities of the tube anode. However, because these lines have a typical Voigt profile and a well defined energy, they can be easily identified and then subtracted from the RAE spectrum. Two peaks of this type were observed in the spectrum of $_{48}$Cd at $25044.9 \pm 1.2$ eV and $25271.4 \pm 0.5$ eV, respectively [see Fig. 5(d)]. These energies coincide within the experimental uncertainties with the energies of the $K\alpha_2$ and $K\alpha_1$ transitions of $_{50}$Sn which are 25044.0 eV and 25271.3 eV, respectively [32]. Since the Cd foil we used for the preparation of the target was certified to contain less than 1 ppm Sn, we attributed the observed contamination to the anode of the x-ray tube.

As our measurements were carried out with solid targets, the valence electrons are not in a single atom potential, but they are affected by the environment of the atom. Many authors have interpreted the peaks appearing in the low energy region of the diagram lines in terms of solid state effects. The solid and chemical effects in the x-ray spectra are reflected in the changes of the transition probabilities and in energy shifts of the transitions in which a valence electron is directly involved. To check the possible influence of solid state ef-

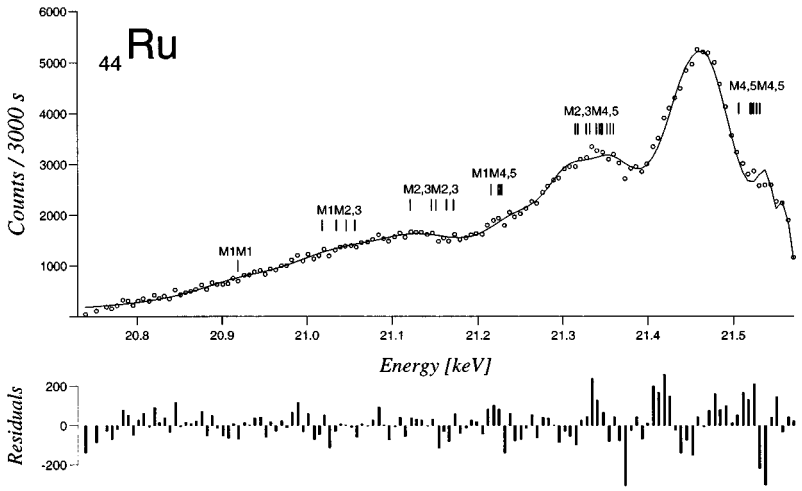


FIG. 6. The fitted ruthenium RAE spectrum (upper part) and the residuals between the measured spectrum and the fitted one (lower part).

fects, we measured a compound of Mo, molybdenumtrioxide ($MoO_3$). The $MoO_3$ target was made in the same way as the Ru one [see Fig. 3(a)]. No significant difference was found between the two spectra (see Fig. 7), indicating that chemical and solid state effects play probably only a minor role in our RAE measurements. The total ($K$-$MM$ RAE)/($K\beta_{1,3}$) relative intensity we got for $MoO_3$ agrees very well with the Mo one, i.e., $(1.14\pm0.09)\%$ for $MoO_3$ and $(1.17\pm0.09)\%$ for Mo.

### B. Radiative Auger effect

According to the shake theory the $M_1M_1$, $M_1M_{4,5}$, and $M_{4,5}M_{4,5}$ final states are forbidden, but not in the configuration interaction (CI) scheme [8]. In fact the $KM_1M_1$ transition is very weak and appears only in some spectra as a small bump showing a very weak CI for this state. The $KM_1M_{4,5}$ is also weak, but in most spectra a small bump lying in the tail of the quite strong $KM_{2,3}M_{4,5}$ transition is observed at the energy corresponding to the ''shake-off-forbidden'' $KM_1M_{4,5}$. Therefore, even when the line is not well resolved a weak CI-contribution cannot be excluded *a priori*. The problem is still more difficult for the $KM_{4,5}M_{4,5}$ transition. To our knowledge, this is the first time that the $M_{2,3}M_{4,5}$ and $M_{4,5}M_{4,5}$ final configurations have been resolved in x-ray emission spectroscopy. For lower $Z$ elements these configurations are either nonexistent because the corresponding subshells are unoccupied, or not resolved because the separation with the main $K\beta_{1,3}$ line is not large enough. For our targets the separation of some hundreds of eV is sufficient for a high resolution instrument. Another problem, however, occurs for these transitions. As for elements above $Z=19$ the $N$ shell starts to be filled, it is also possible that $K$-$MN$ RAE's take place instead of $K$-$MM$. Unfortunately the $K$-$MN$ RAE transitions of the lowest energy overlap with the $K$-$MM$ of the highest energy. As the edges of the individual transitions cannot be resolved clearly, it is not possible to distinguish these two transitions. According to Scofield's theoretical predictions the total $K$-$MN$ intensity should, however, be smaller than the $K$-$MM$ one, at least for the measured elements [11].

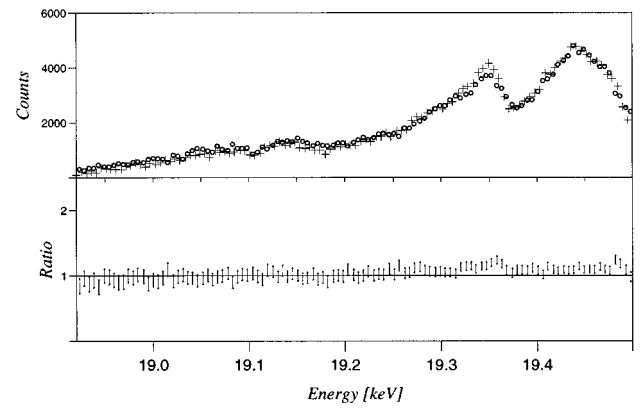


FIG. 7. Comparison of the $K$-$MM$ RAE yields of Mo and $MoO_3$ (+ = $MoO_3$, ○ = Mo). The lower part of the figure shows the ratio of the two spectra.

The theoretical energies of the $K$-$MM$ and $K$-$MN$ transitions appearing in our spectra are indicated by small bars, see Figs. 5(a)–5(e). These theoretical energies are in fact semiempirical Auger electron energies. The edge energy of a RAE transition, when the final state of the ejected electron is just above the Fermi level, is identical with the Auger electron energy relative to the Fermi level, since the interaction of the outgoing electron with the hole is small. As the experimental $K$-$M_iM_j$ Auger electron energies are hardly found in the literature, we used the following approximation, which is also generally used by other authors:

$$E(K-M_iM_j)=E(K\alpha_1)+E(L_3M_iM_j), \tag{4}$$

where $E(K\text{-}M_iM_j)$ are the approximate radiative Auger energies, $E(K\alpha_1)$ the energy of the $K\alpha_1$ emission line, and $E(L_3M_iM_j)$ the energy of Auger electrons referred to the Fermi level.

Since the separation of $K$-$MM$ and $K$-$MN$ becomes larger with increasing $Z$, we also measured the RAE region for a metallic gadolinium target. The purpose of the gadolinium measurement was to highlight the difficult problem of the $K$-$M_{4,5}M_{4,5}$ analysis. For this element the $K$-$MM$ and $K$-$MN$ RAE are not overlapping. Peaks could be observed, as expected, at energies corresponding to the $K$-$M_{2,3}N_{1,2,3}$ and $K$-$M_{2,3}N_{4,5}$ RAE transitions (see Fig. 8). There is also a very small bump appearing in the energy region where the $K$-$M_1N_{1,2,3}$ transitions are expected. Further, one finds below the $K$-$MN$ structure a quite well resolved peak at the ener-

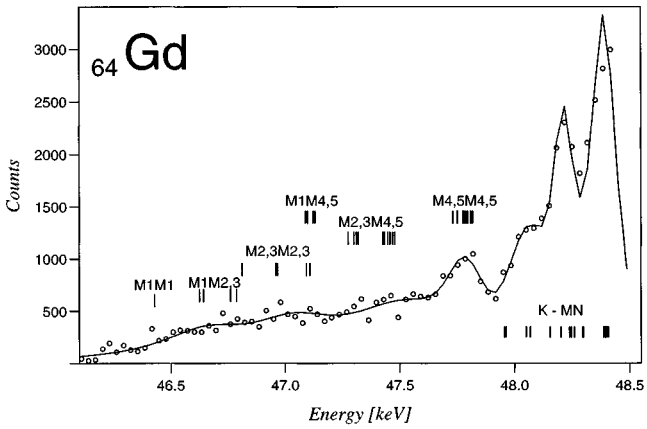


FIG. 8. Comparison of the *K-MM* and *K-MN* RAE yields of Gd.

gies of the $K$-$M_{4,5}M_{4,5}$ transitions. As its intensity is stronger than that of the not well resolved $K$-$M_{2,3}M_{4,5}$ and as the line shape is typical of the RAE type, we believe that the strong, asymmetric peak above $K$-$M_{2,3}M_{4,5}$ is for all targets principally due to $K$-$M_{4,5}M_{4,5}$ transitions. A small part of this peak is, however, probably due to the tails of the quite strong $K$-$M_{2,3}N_{1\ldots5}$ transitions. Nevertheless, in the determination of the total *K-MM* RAE yield, this *K-MN* contribution, which was estimated to be less than about 4%, was not considered.

Because a RAE group consists of many components, we have listed in Table II only the experimental edge energies of the strongest transitions. For each group the selection of the strongest line was based on the *L-MM* Auger transition rates given by Chen [33], who has included in his calculations relativistic and correlation effects. Some Auger transition energies are also given in Chen's study but not, unfortunately, for the elements investigated in our experiment. The theoretical energies quoted in Table II were therefore taken from Larkins [12]. Comparing Larkins's predictions to our experimental edge energies, one can see that there are some important discrepancies which have theoretical and experimental explanations. First in Larkins's calculations, relativistic and correlation effects are not included. A comparison of Larkins' and Chen's values for $_{45}$Rh and $_{60}$Nd shows that the inclusion of these effects results in Auger energies which are from about 5 eV up to 25 eV lower than those of Larkins. In addition, we compared our edges to the energies of the strongest nonradiative Auger transitions, which do not coincide necessarily with the strongest radiative transitions. From the experimental side the determination of the edges, which are smeared out by the instrumental resolution and partly masked by the tails of other RAE transitions, is quite difficult. Therefore, the experimental values are also characterized by large errors of typically 10 eV or more. For these reasons and because Eq. (4) is a crude approximation, we are inclined to conclude that our energies are in satisfactory agreement with Larkins's predictions.

TABLE III. Extracted ratios for *K-MM* RAE to $K\beta_{1,3}$. The given theoretical values were interpolated from the predictions given by Scofield's RHF theory [11].

| Element | Ratio $\frac{I(K-MMRAE)}{I(K\beta_{1,3})}$ Experimental intensity ratio (in %) | Interpolated ratio from theory (in %) |
|---|---|---|
| $_{42}$Mo | 1.14 ± 0.09 | 1.34 |
| $_{44}$Ru | 1.36 ± 0.09 | 1.16 |
| $_{46}$Pd | 0.99 ± 0.08 | 1.00 |
| $_{48}$Cd | 0.46 ± 0.07 | 0.86 |
| $_{50}$Sn | 0.36 ± 0.05 | 0.75 |

To determine the intensity ratio $I(K\text{-}MM)/I(K\beta_{1,3})$, we added the intensities of all Voigt functions used to fit the *K-MM* spectrum. Voigt profiles lying above the theoretical $KM_{4,5}M_{4,5}$ energies were not taken into account. The yields were not corrected for the self-absorption in the target, nor for the intensity attenuation by the crystal. These corrections were found to be smaller than 1% (respectively 2%) for the heaviest (respectively lightest) element and thus not considered. The so-obtained ratios for the total *K-MM* RAE intensities are given in Table III. They are also presented and compared to already existing experimental data in Fig. 9. Regarding this figure one can see that for low-$Z$ elements there is an obvious tendency of the theory to overestimate the *K-MM* intensities. The intensity we found for palladium agrees very well with the theoretical value. This is perhaps due to the fact that palladium has a configuration with filled subshells. For Cd and Sn, we found a smaller value than the one predicted by the theory, as in the low-$Z$ experiments. For ruthenium, on the contrary, the experimental value is larger than the theoretical one. A careful examination of the Ru spectrum did not reveal any anomaly, such as the presence of

TABLE II. Comparison between experimental RAE edge energies and semiempirical Auger electron energies of Larkins [12]. All energies are in eV. The values marked with * could not be determined, due to insufficient intensity.

| Final state | Target $_{42}$Mo | | $_{44}$Ru | | $_{46}$Pd | | $_{48}$Cd | | $_{50}$Sn | |
|---|---|---|---|---|---|---|---|---|---|---|
| | Expt. | Theor. | Expt. | Theor. | Expt. | Theor. | Expt. | Theor. | Expt. | Theor. |
| $M_4M_5\ ^1G_4$ | 19502 | 19511 | 21501 | 21520 | 23622 | 23638 | 25833 | 25855 | 28154 | 28178 |
| $M_2M_5\ ^1F_3$ | 19365 | 19328 | 21356 | 21318 | 23463 | 23418 | 25636 | 25614 | 27953 | 27915 |
| $M_1M_4\ ^1D_2$ | 19247 | 19234 | 21220 | 21215 | 23306 | 23305 | 25502 | 25491 | * | 27783 |
| $M_2M_3\ ^1D_2$ | 19158 | 19172 | 21144 | 21146 | 23237 | 23230 | 25409 | 25410 | 27732 | 27695 |
| $M_1M_3\ ^3P_2$ | 19089 | 19089 | * | 21056 | 23133 | 23133 | * | 25305 | 27577 | 27582 |
| $M_1M_1\ ^1S_0$ | * | 18964 | * | 20919 | * | 22980 | * | 25136 | * | 27397 |

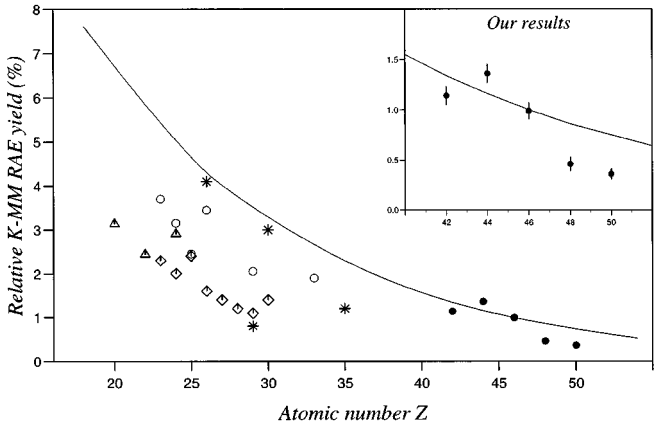


FIG. 9. Comparison of published experimental data of relative $I(K\text{-}MM)/I(K\beta_{1,3})$ intensity ratios with theory, as a function of $Z$. The solid line is an interpolation of theoretical values from Scofield's RHF theory [11]. ●, this work; ◇, Servomaa *et al.* [25,26]; *, Marageter *et al.* [38]; △, Budnar *et al.* [39]; ○, Campbell *et al.* [40].

trace element lines or Raman scattering peaks. In fact, the spectrum is very similar to the ones of the neighbor elements, Mo and Pd. The results for Mo and Ru which are, respectively, smaller and larger than the theoretical predictions seem thus to be somewhat contradictory. It is, however, possible that this apparent inconsistency results from the electronic configuration of these elements, both of which have two unfilled subshells in the ground state. Final state configurations are then characterized by three open shells. In such cases, large correlation effects that could be responsible for the above mentioned inconsistency are expected at least when outer shells are involved in the Auger transition [34].

From RAE measurements it is in principle possible to extract the partial shake probabilities corresponding to the different subshells. This method is not very precise, mainly because of the unknown analytical shape of the extended RAE structures. Theoretical predictions for partial shake probabilities are also scarce, especially for medium-mass elements. As the ratio of these subshell shake probabilities is not expected, however, to vary rapidly with the atomic number $Z$, we have compared the $3d/3p$ shake probability ratio extracted from our $K\text{-}MM$ RAE measurement of $_{46}$Pd with the results of recent calculations performed for $_{36}$Kr. Two different theoretical approaches predict for this element $3d/3p$ shake ratios of 2.67 and 3.15 [35], respectively, both values in good agreement with our experimental result of 2.95. The first theoretical value was obtained from the sudden approximation model using HFS wave functions [36], the second from full Dirac-Fock (DF) calculations in the dipole approximation [37].

## V. CONCLUSION

In the present experiment $K\text{-}MM$ RAE transitions of five medium-mass elements ranging from molybdenum ($Z=42$) to tin ($Z=50$) were measured by means of high resolution crystal diffractometry. Several groups of RAE transitions could be identified. The RAE edge energies extracted from our experiment were found to be in satisfactory agreement with calculated Auger transition energies. For a more detailed comparison improved calculations using explicit CI are needed. Total $I(K\text{-}MM$ RAE$)/I(K\beta_{1,3})$ yield ratios were also determined. Except for ruthenium and palladium, we observed that theory overestimates the RAE intensities. A similar conclusion was drawn from previous measurements performed on low-$Z$ elements. Our results show, however, that the discrepancies are smaller for mid-$Z$ atoms. For palladium a good agreement was found. For this element the ratio of the probabilities for a shake process in the $3d$ and $3p$ subshells as a result of a $K$-shell photoionization could be extracted from the RAE spectrum. The obtained value was compared to results of calculations performed for krypton, the single mid-$Z$ element for which theoretical values could be found in the literature. A quite acceptable agreement was found in this case, too. The large RAE intensity observed for ruthenium could not be explained clearly and was tentatively attributed to correlation effects. The latter seem to play an important role in the calculation of RAE yields and RAE energies, especially when the initial and final state configurations are characterized by several open subshells. As a concluding remark we would like to point out that progress in the RAE theory is highly desirable. In particular, a better knowledge of the analytical shape of the RAE transitions would be very helpful for the analysis and the interpretation of the experimental spectra.

## ACKNOWLEDGMENT

This work was partially supported by the Swiss National Science Foundation.

[1] M. Budnar and A. Mühleisen, Nucl. Instrum. Methods B **75**, 81 (1993).
[2] R. Manne, Chem. Phys. Lett. **5**, 125 (1970).
[3] F. Hopfgarten and R. Manne, J. Electron. Spectrosc. **2**, 13 (1973).
[4] F.R. McFeely *et al.*, Phys. Rev. B **9**, 5268 (1974).
[5] F. Bloch and P.A. Ross, Phys. Rev. **47**, 884 (1935).
[6] F. Bloch, Phys. Rev. **48**, 187 (1935).
[7] T. Åberg and J. Utriainen, Phys. Rev. Lett. **22**, 1346 (1969).
[8] T. Åberg, Phys. Rev. A **4**, 1735 (1971).
[9] M.O. Krause, T.A. Carlson, and R.D. Dismukes, Phys. Rev. **170**, 37 (1968).
[10] T. Åberg, *Atomic Inner-Shell Processes*, edited by B. Crasemann (Academic, New York, 1975), p. 353.
[11] J.H. Scofield, Phys. Rev. A **9**, 1041 (1974).
[12] F.P. Larkins, At. Data Nucl. Data Tables **20**, 311 (1977).
[13] B. Perny *et al.*, Nucl. Instrum. Methods A **267**, 120 (1988).
[14] W. Beer, P.F.A. Goudsmith, and L. Knecht, Nucl. Instrum. Methods **219**, 322 (1984).
[15] R.C. Sharma *et al.*, Nucl. Instrum. Methods **130**, 305 (1975).

[16] J.A. Bearden and A.F. Burr, Rev. Mod. Phys. **39**, 78 (1967).
[17] F. James and M. Roos, Comput. Phys. Commun. **10**, 343 (1975).
[18] C.J. Batty, S. D. Hoath, and B. L. Roberts, Nucl. Instrum. Methods **137**, 179 (1976).
[19] K.S. Kölbig, Commun. ACM **15**, 465 (1972).
[20] E.G. Kessler *et al.*, Nucl. Instrum. Methods **160**, 435 (1979).
[21] K.A. Jamison *et al.*, Phys. Rev. A **14**, 937 (1976).
[22] K.A. Jamison, J.M. Hall, and P. Richard, J. Phys. B **8**, L458 (1975).
[23] T. Suzuki, J. Phys. Soc. Jpn. **22**, 1139 (1967).
[24] C.J. Sparks, Jr., Phys. Rev. Lett. **33**, 262 (1974).
[25] O. Keski-Rahkonen and J. Ahopelto, J. Phys. C **13**, 471 (1980).
[26] A. Servomaa and O. Keski-Rahkonen, J. Phys. C **8**, 4124 (1975).
[27] J. Kawai *et al.*, Analyst **119**, 601 (1994).
[28] T. Mukoyama and K. Taniguchi, Phys. Rev. A **36**, 693 (1987).
[29] M.H. Chen, B. Crasemann, and H. Mark, Phys. Rev. A **25**, 391 (1982).
[30] B. Boschung *et al.*, Phys. Rev. A **51**, 3650 (1995).
[31] J.H. Scofield, At. Data Nucl. Data Tables **14**, 121 (1974).
[32] K.D. Sevier, At. Data Nucl. Data Tables **24**, 359 (1979).
[33] M.H. Chen, Phys. Rev. A **31**, 177 (1985).
[34] K.G. Dyall and F.P. Larkins, J. Phys. B **15**, 1811 (1982).
[35] T. Mukoyama and Y. Ito, Nucl. Instrum. Methods B **87**, 26 (1994).
[36] T. Mukoyama and Y. Ito, Bull. Inst. Chem. Res., Kyoto Univ. 71(6) (1993).
[37] D.L. Wark *et al.*, Phys. Rev. Lett. **67**, 2291 (1991).
[38] E. Margeter, W. Wegscheider, and K. Müller, X-Ray Spectrom. **13**, 78 (1984).
[39] M. Budnar *et al.*, Nucl. Instrum. Methods B **63**, 377 (1992).
[40] J.L. Campbell *et al.*, Phys. Rev. A **33**, 2410 (1986).